

A Self-Powered Triboelectric Hybrid Coder for Human–Machine Interaction

Yu Cao, Yuan Yang, Xuecheng Qu, Bojing Shi,* Lingling Xu, Jiangtao Xue, Chan Wang, Yuan Bai, Yansong Gai, Dan Luo,* and Zhou Li*

Human–machine interfaces have penetrated various academia and industry fields such as smartphones, robotic, virtual reality, and wearable electronics, due to their abundant functional sensors and information interaction methods. Nevertheless, most sensors' complex structural design, monotonous parameter detection capability, and single information coding communication hinder their rapid development. As the frontier of self-powered sensors, the triboelectric nanogenerator (TENG) has multiple working modes and high structural adaptability, which is a potential solution for multi-parameter sensing and miniaturizing of traditional interactive electronic devices. Herein, a self-powered hybrid coder (SHC) based on TENG is reported to encode two action parameters of touch and press, which can be used as a smart interface for human–machine interaction. The top-down hollow structure of the SHC, not only constructs a compositing mode to generate stable touch and press signals but also builds a hybrid coding platform for generating action codes in synergy mode. When a finger touches or presses the SHC, Morse code and Gray code can be transmitted for text information or remote control of electric devices. This self-powered coder is of reference value for designing an alternative human–machine interface and having the potential to contribute to the next generation of highly integrated portable smart electronics.

interaction platforms that improve the quality of life and work have been derived, such as smartphones,^[5] robots,^[6–8] virtual reality,^[9–11] wearable electronics,^[12–14] and so on. Therein, the human–machine interface plays the role of a bridge between human civilization and the digital world.^[15] One of the foundations of the human–machine interface is sensors with multiple functions, which recognize the physiological indicators or physical parameters of the human body and convert them into electronic signals for transmission, such as fingerprint features,^[16] strain,^[17] vibration,^[18] and inertia.^[19] These sensors can accurately feedback instantaneous information, but few of them have achieved detecting multiple parameters. To achieve multi-parameter monitoring and interaction, a general approach is increasing the number of the devices, however, this will increase the energy consumption and the additional volume.

Meanwhile, some alternative methods have been demonstrated to realize a more efficient human–machine interface, among them self-powered devices.^[20] The self-powered devices are based on piezoelectric or triboelectric effects, which can convert external force into electricity directly.^[21] In other words, they are able to act as self-powered interfaces to transfer human mechanical signals into

1. Introduction

The rapid development of the Internet of Things has made the connection between humans and electronic products increasingly close.^[1–4] As a result, a large number of information

Y. Cao, Y. Bai, Y. Gai, Z. Li
Center on Nanoenergy Research
School of Physical Science and Technology
Guangxi University
Nanning 530004, China


Y. Yang, X. Qu, B. Shi, L. Xu, J. Xue, C. Wang, D. Luo, Z. Li
Beijing Key Laboratory of Micro-nano Energy and Sensor
Beijing Institute of Nanoenergy and Nanosystems
Chinese Academy of Sciences
Beijing 101400, China
E-mail: luodan@binn.cas.cn; zli@binn.cas.cn

Y. Yang, X. Qu, Z. Li
School of Nanoscience and Technology
University of Chinese Academy of Sciences
Beijing 100049, China

B. Shi
Beijing Advanced Innovation Centre for Biomedical Engineering
Key Laboratory for Biomechanics and Mechanobiology
of Ministry of Education
School of Biological Science and Medical Engineering
Beihang University
Beijing 100191, China
E-mail: bjshi@buaa.edu.cn

J. Xue
Institute of Engineering Medicine
Beijing Institute of Technology
Beijing 100081, China

Z. Li
Institute for Stem Cell and Regeneration
Chinese Academy of Sciences
Beijing 100101, China

 The ORCID identification number(s) for the author(s) of this article can be found under <https://doi.org/10.1002/smt.202101529>.

DOI: 10.1002/smt.202101529

electrical signals. Due to their unique properties, self-powered devices have achieved some great achievements: ultrasensitive monitoring of physiological and psychological signs,^[22–24] recognition of motions and activities,^[25–27] personalized products,^[28–30] and so on. As an important member of the self-powered devices, triboelectric nanogenerator (TENG) has high structural adaptability and four basic working modes, attracting more and more attention from scholars. Some researchers have proposed the use of TENG to control portable electronic devices, including smart gloves,^[31–33] electrodes with special patterns,^[34–37] and flexible fabrics.^[38–40] These studies have verified the efficiency and convenience of using TENG as a human–machine interface.

Here in this work, we demonstrate a self-powered hybrid coder (SHC) based on TENG as a multifunctional human–machine interface. Compared with other reported TENG-based coding devices,^[41–45] the SHC has two working modes: single-electrode mode and contact-separation mode, which can convert two action signals of finger touch and press into two different coding formats, Morse code and Gray code. The unique generation method of hybrid signal determines the particularity of coding definitions, which forms an integrated coding platform for hybrid transmission of multiple coded signals. This subtle way allows the SHC to adapt to a variety of human–machine interaction signals, which greatly expands the application space of it. The appearance and size of SHC is like a button, which can be used on various occasions and equipment. Then, we presented two typical application scenarios of SHC, including smart control of a pilot lamp and a remote car. The potential coding approach of the SHC might be extended to more fields such as smart wear, information security, virtual reality (VR), augmented reality (AR), and robotics.

2. Results and Discussion

2.1. Structure and Working Principle of SHC

As schematically illustrated in **Figure 1a**, the SHC can detect the two action parameters of touch and press, due to its simple structural design that is stacked up and down and hollow in the middle. This structure perfectly combines the two modes of the single-electrode (SE) and the contact-separation (CS) mode. The SHC is manufactured by physical methods (**Figure S1**, Supporting Information). The SE part of the SHC is composed of a Kapton film and an Al electrode. Correspondingly, the CS part is constituted by a stainless steel shrapnel, a polytetrafluoroethylene (PTFE) film, a Cu electrode, and a polyethylene glycol terephthalate (PET) film that is used as a substrate. The SHC is prepared by bonding the SE part and the CS part through a polyester tape, which plays the role of insulation and adhesion. (**Figure S2**, Supporting Information). In particular, SUS301 is selected as the material of the stainless steel shrapnel, due to its advantages of certain conductivity, outstanding fatigue resistance, corrosion resistance, and resilience compared with other metal materials. It is enough to support the structure of the SE part, while providing a source of charge for the CS electrical signal generated by the pressing action. In addition, it can ensure immediate rebound at the end of the pressing action, without affecting the generation of the next pressing electrical signal. **Figures S3 and S4** (Supporting Information) display the micrographs of stainless spring steel and

the SEM characterization of PTFE before and after magnetron sputtering, respectively. After processing, a dense copper film with a thickness of about 120 nm is formed on the surface of the PTFE. It could be seen from the microstructure that the flat and dense triboelectric layer surface guarantees the stability of the device's performance to the greatest extent. Moreover, the SHC has a diameter of about 10 mm, a thickness of 1 mm, and a mass of less than 0.7 g (**Figure S5**, Supporting Information). Miniaturization makes its application scenarios broad, and its easy-to-process feature allows it to be further designed and developed.

Independent detection of touch and press is the basic mode of the SHC (**Figure 1b**). The recognition of the touch action is based on the SE working mode of TENG, which is attributed to the changing electric field between the finger and the Kapton film during the touch action. An electrostatic induction will induce electrical signals between the Al electrode and the ground. The voltage signal of the touch action at a frequency of 1 Hz verifies the sensitivity and stability in this mode. Similarly, when only the press action is recognized, an alternating electrostatic field appears between the stainless steel sheet and the PTFE film, inducing electrons to transfer between the stainless steel sheet and the Cu electrode to generate an electrical signal in the CS mode. When the pressing frequency is 1 Hz, the voltage signal remains stable.

In the synergy mode, the cooperation of the two action parameters can derive many signals for encoding and control. **Figure 1c** reveals the transfer of electrons and the generation of signal waveforms in a complete action of touch-press-bounce-off. When the finger approaches the SHC down, the SE signal is triggered (**Figure 1c(i)**). Until it is thoroughly attached to the Kapton surface, the SE signal disappears. This process produces a positive pulse signal. Then, the finger continues to press down to force the stainless steel sheet to deform close to the PTFE, and the CS signal is triggered (**Figure 1c(ii)**) to generate a forward voltage signal. When the two surfaces are in full contact, the CS signal disappears. As the finger releases the pressure, the stainless steel rebounds and the electrons return to produce a negative CS signal (**Figure 1c(iii)**). When the stainless steel returns to the initial position, the CS signal disappears completely. Finally, when the finger is removed from the SHC, the negative SE signal is activated (**Figure 1c(iv)**), and finally forms a complete cycle with the positive SE signal. The multiple application modes of SHC enable it to adapt to a considerable number of application scenarios, especially in the areas of intelligent interaction, security warning, and remote control (**Figure 1a**).

2.2. Output Performance Characterization of SHC under SE Mode

A single-electrode mode TENG is fabricated at the outmost layer of the SHC to detect touch action. A Kapton film serves as the triboelectric layer to exchange charges with the finger. The Kapton film and the skin have a significant difference in electronegativity according to the triboelectric series,^[46] so the electron transfer is extremely easy to occur when they are in contact. An Al electrode is used to respond to electrostatic induction caused by the triboelectric effect and generate alternating signals (**Figure 2a**). When contact occurs, the transfer of electrons between the interfaces causes the finger and Kapton

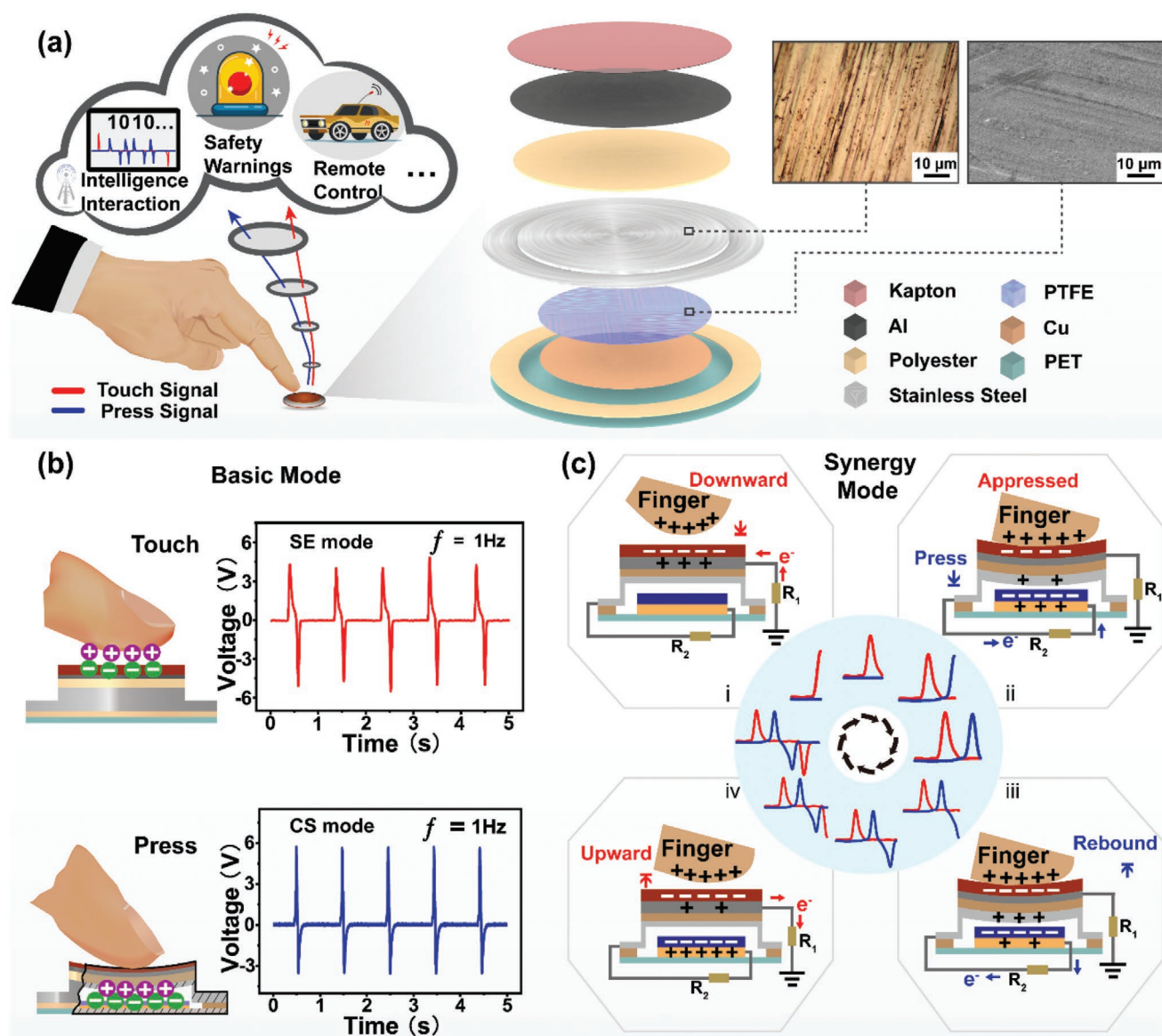


Figure 1. Overview diagram of SHC. a) 3D structure of SHE and its application in intelligence interaction, safety warnings, and remote control. b) Charge transfer process and voltage signal of single-electrode (SE) mode and contact-separation (CS) mode corresponding to touch action and press action, respectively. c) Process of synergistic signal generation of SHC in an ordinary moving cycle.

to bind equal amounts of opposite charges, respectively. Once the finger moves away from the device, the electrical properties of the two surfaces will change at the same time, and the finger is positively charged due to the loss of electrons. As the finger leaves away from Kapton film, the finger will always remain positively charged. This makes the negative triboelectric charges on the Kapton surface not compensated, and eventually induces electrons to be driven from the aluminum electrode to the ground to balance the electrostatic field. When the fingertip touches the device again, the reduced electrostatic field supplies conditions for the backflow of electrons from the ground to the Al electrode. Until the finger and Kapton film return to their original contact state, the electron stops moving. This cyclical action generates an alternating current (AC) in the external circuit.

The relationship between the touch parameter and the device performance was studied in detail. The open-circuit voltage (V_{OC}) and the short-circuit current (I_{SC}) were measured at the frequency of 3 Hz, and the pressure column pasted with pig-skin was kept at a distance of 2 cm from the SHC (Figure S6, Supporting Information). The values of V_{OC} and I_{SC} are ≈ 6 V and 0.4 μ A, respectively (Figure 2b,c). Then, we tested the outputs of the SHC under SE mode when connected with different external loads. As the load resistance increases, the voltage presents an enhancement while the current delivers an opposite variation (Figure 2d). When the external resistance is 70 M Ω , the peak power value reaches ≈ 0.6 μ W (Figure S7, Supporting Information). It means that the single-electrode mode TENG has a relatively large internal resistance and a small output charge density. For SHC application, it is more suitable

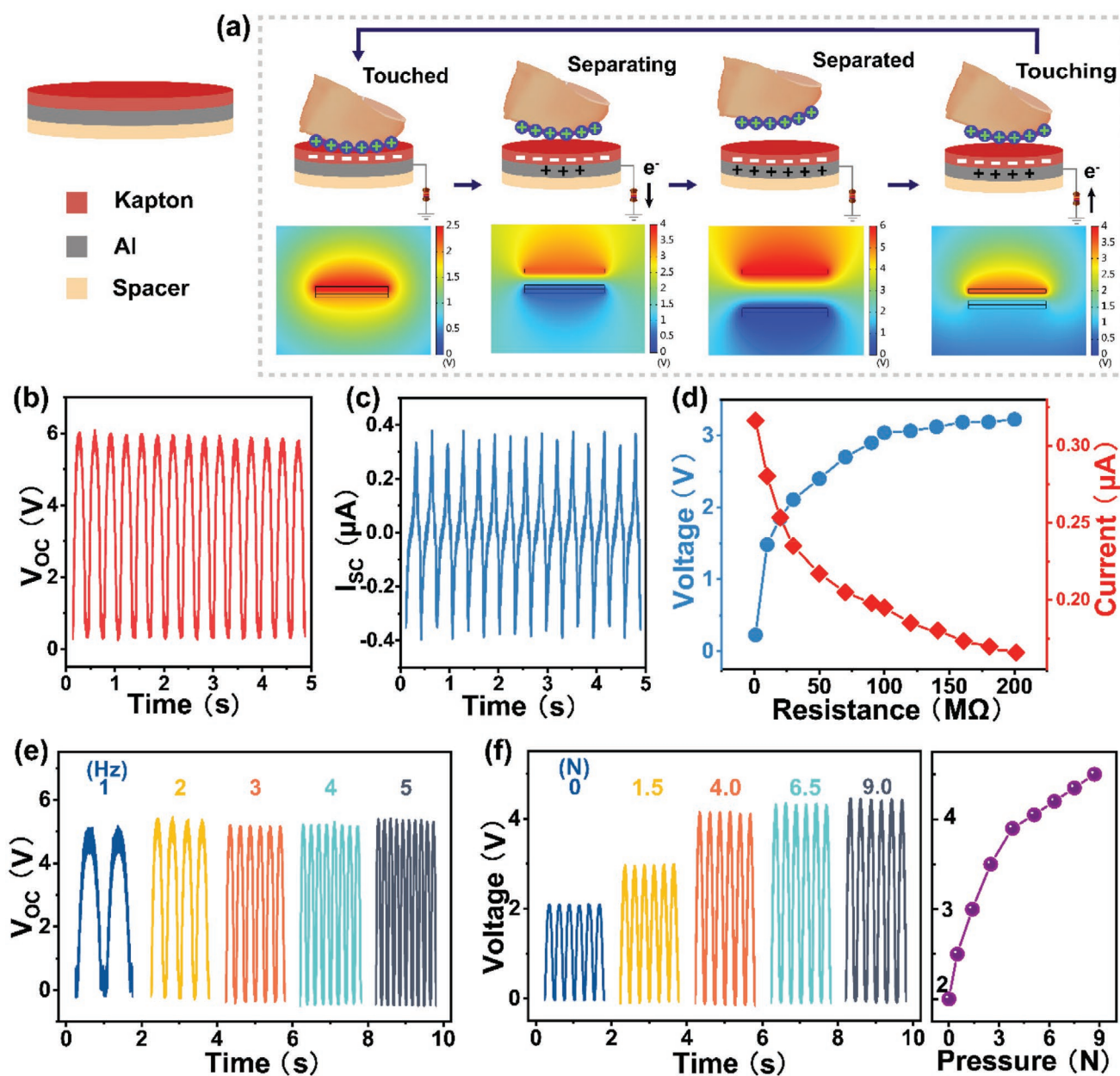


Figure 2. Electrical characterization of the SHC under SE mode. a) Working mechanism and COMSOL software simulation of SHC in the SE mode section. b,c) Open-circuit voltage and short-circuit current at the frequency of 3 Hz. d) Output voltage and current under the different external load resistances. e) Open-circuit voltage at different frequencies. f) Output voltage at different pressures and relation curve between force and electricity.

to be used as a small signal self-powered sensor rather than an energy harvester to power electronic devices. At the relative distance of 2 cm and the force of 6 N, the V_{OC} and Q_{SC} remain relatively stable as the touch speed increases stepwise from 1 to 5 Hz (Figure 2e and Figure S8, Supporting Information). The reason is that the charge accumulated in the triboelectric layer is saturated, which makes the induced potential difference of the back electrode remain stable in each cycle. The I_{SC} increases with frequency, rising from 0.15 μA at 1 Hz to 0.75 μA at 5 Hz. This is because the increased contact and separation rate results in a fast flow rate of charges.^[47] Figure 2f reveals

the relationship between the output voltage and the pressure applied to the TENG. As the pressure rises from 0 to 9 N, the voltage becomes higher due to the larger effective contact area and triboelectric charge density.^[48] Furthermore, the prominent stability is testified by the long-term operation (Figure S9, Supporting Information). During 30 000 cycles, the overall situation is satisfactory, and a slight increase of voltage could be acceptable, resulting from the constant accumulation of electric charge and uncontrollable man-made disturbances. These results indicate the SE part of SHC is of potential durability and high reliability.

2.3. Output Performance Characterization of SHC under CS Mode

The electrical signal under CS mode is mainly used to identify press action. As shown in **Figure 3a**, the stainless steel shrapnel and PTFE are used as the triboelectric layer in the CS mode, and the surfaces of the two will contact and separate with the

pressing action. PET is used as the base to carry all the units. A 3M polyester tape plays an important part in fixing and isolating the triboelectric layers. A more detailed fabrication process is presented in the Experimental Section. The contact separation signal is caused by the coupling effects of the triboelectrification and electrostatic induction, the working mechanism is briefly

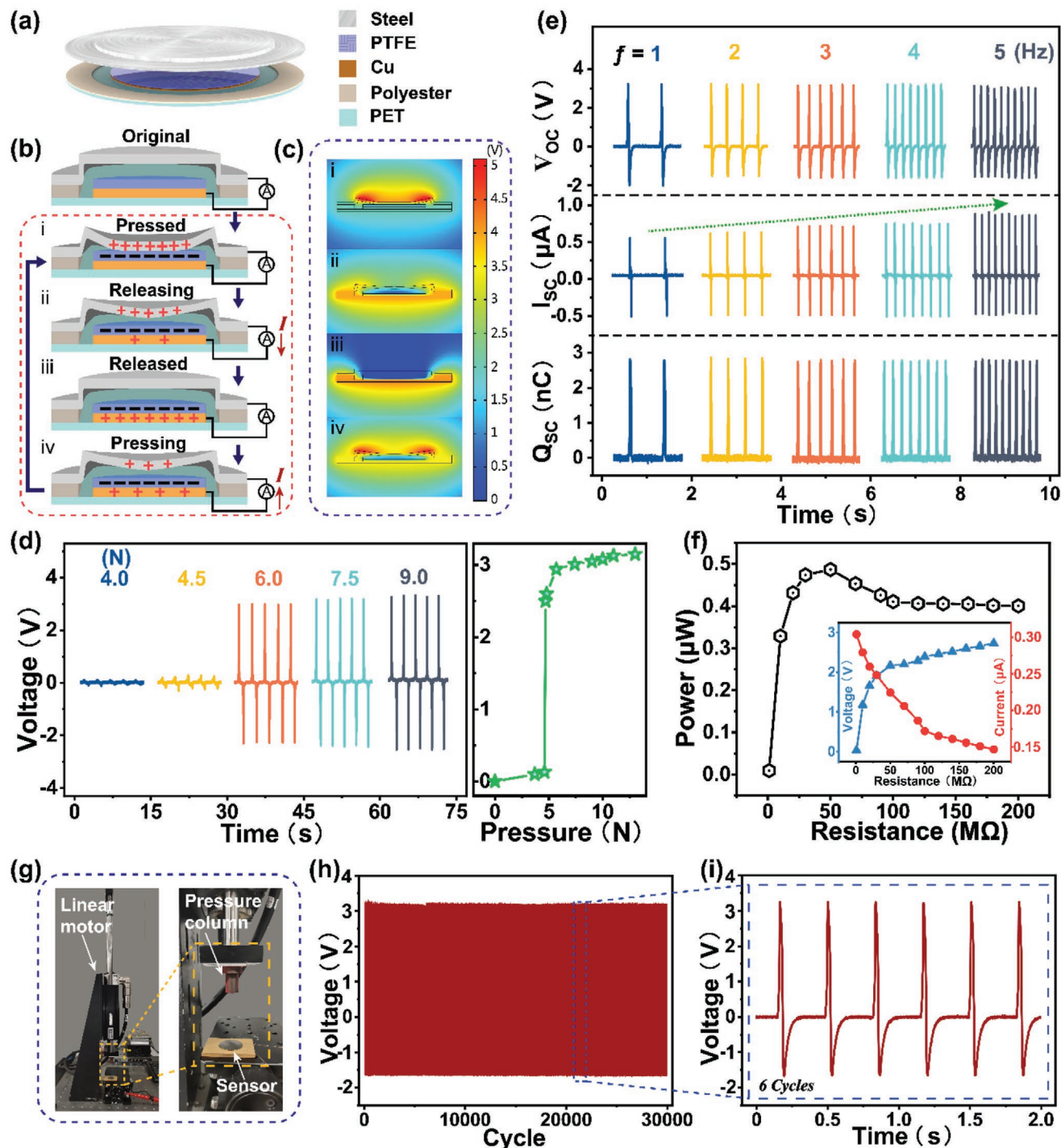


Figure 3. Output performance characterization of SHC under CS mode. a) Sketch of SHC in the CS mode section. b,c) Operating principle and imitated diagram of COMSOL software. d) Output voltage in terms of different forces at $f = 3$ Hz. e) Open-circuit voltage, short-circuit current, and transferred charge at different frequencies. f) Output voltage, current, and power under the different external load resistances. g–i) Platform and output property of durability test.

depicted in Figure 3b. Initially, since the spring steel film and the PTFE film are not in contact, there is no change in the surface charges on them, therefore no electrostatic field is generated. When a vertical force loads on the spring steel film to make a contact with the PTFE film, a charge exchange occurs between the surfaces of these two materials due to the different charge capture capabilities (Figure 3b(i)). According to the triboelectric series of materials,^[46] steel tends to lose electrons easier than PTFE. When the external force disappears, an electric potential difference will appear between the two triboelectric layers along with the spring steel bounces back causing a separation of them. Electrostatic force induces the flow of electrons between the copper electrodes on the back of the PTFE and the spring steel, generating a current (Figure 3b(ii)) to balance the resulting electrostatic field. Until the spring steel returns to its original position (Figure 3b(iii)), the electrostatic field in the space reaches a stable state and there is no more electron transfer between the back electrodes. The insulating properties of PTFE will make the charge remain for quite some time. Once there is pressure again to deform the spring steel downwards, the field balance will be broken. As the electric potential difference is reduced, the electron flow between the spring steel and the copper electrode will be reversed than before, until the two triboelectric materials come into contact again to make the electrostatic field disappear (Figure 3b(iv)). This alternating current signal generated by this contact-separation mode will cyclically occur according to the pressing action. Then, the COMSOL software has been used to simulate this model (Figure 3c), where the results are consistent with the analysis above.

To further systematically evaluate the output capability and stability of the output signals of the SHC, an experimental platform was set up by integrating the mechanical and electrical measurement systems (Figure S10a,b, Supporting Information). The force gauge is used to make the spring steel film be deformed downward by a gradual distance, then the information between displacement, force and voltage is recorded. The processed data is presented in the 3D chart of Figure S11 (Supporting Information). It is noticed that when the deformation of the spring steel film is less than 0.7 mm, the voltage signal is too small to be recorded. Until the amount of deformation reaches 0.7 mm, an electrical signal peak emerges suddenly, with the voltage amplitude is 2.6 V and the force is 4.8 N. It is inferred that the shrapnel deformed and contacted the PTFE below, then contact-electrification occurred. To verify this idea, we used a linear motor and a push-pull force gauge to measure the voltage signal under different forces at a frequency of 3 Hz. The result of the force electric signal verifies the above conjecture, and shows that the CS signal can be controlled by an external force like a switch. The voltage signal of the SHC shows a positive correlation with pressure (Figure 3d). When the pressure is lower than 5 N, the two triboelectric layers are difficult to contact. The signal output is almost invisible. When the stainless steel shrapnel is pressed down with a force of about 5 N, the two triboelectric layers contact, and the voltage output increases sharply. As the pressure increases, the limited contact area causes the V_{OC} to grow slowly.

The frequency of touching and pressing is one of the key factors to influence the electrical outputs of the SHC. For a deeper analysis of the relationship between the frequency and electrical

outputs, the frequency of pressing is increased from 1 to 5 Hz when the pressure is 7 N. In this case, the V_{OC} , I_{SC} , and the transferred charges (Q_{SC}) were measured separately (Figure 3e). The V_{OC} and Q_{SC} changed little at different frequencies, which kept at ≈ 3 V and ≈ 3 nC, respectively. But, the I_{SC} showed a trend of positive correlation with frequency, increasing from 0.5 to 0.8 μ A. The parameters of the contact-separation mode can be analyzed by the plate capacitance model, which is defined by the electrodynamic theory as follows

$$V_{OC} = \frac{\sigma x(t)}{\epsilon_0} \quad (1)$$

$$Q_{SC} = \frac{S\sigma x(t)}{d_0 + x(t)} \quad (2)$$

Here, σ is the surface charge density carried on the surface of different materials after contact, $x(t)$ is the distance between the two triboelectric surfaces, ϵ_0 and d_0 are the vacuum dielectric constant and effective thickness constant, respectively, and S is the effective contact area. It is easy to infer from the formula (1) and (2) that once the material properties and the contact area are stated, V_{OC} and Q_{SC} are only related to the distance $x(t)$. The position of the pressure column is fixed in this experiment, so the values of V_{OC} and Q_{SC} are approximately constant. For the I_{SC} , it can be defined as

$$I_{SC} = \frac{Q_{SC}}{\Delta(t)} \quad (3)$$

The intensity of I_{SC} is inversely proportional to the time interval of charge change, in other words, it will become larger as the frequency increases. According to the data and theoretical analysis, it can be concluded that the compression speed will affect the magnitude of the current instead of disturbing the amplitude output of the signal. It proves that the SHC works reliably in a variety of pressing frequencies.

Meanwhile, the outputs of the SHC are largely dependent on the external load resistances. Figure 3f exhibited the current decreases while the voltage indicates a contrary trend as the load resistance increases from 1 to 200 M Ω . And a maximum power of 0.48 μ W was achieved when the load resistance was 50 M Ω . Moreover, durability is a crucial condition that must be considered for most sensors. We used a linear motor to do a fatigue test for the SHC (Figure 3g). After 30 000 cycles of contact-separation at $f = 3$ Hz, the signal has no obvious attenuation (Figure 3h,i). The difference between the positive and negative peaks of the waveform is due to the structure of the spring steel and the impact of the linear motor. The same integral area demonstrates that the amount of electrons transferred in each cycle is the same. For the SHC, it brings a convincing performance overall in contact-separation working mode.

2.4. Hybrid Encoding and Decoding Process of SHC

The SHC provides a platform for hybrid coding of SE signal and CS signal. The two types of signal are coupled and transmitted

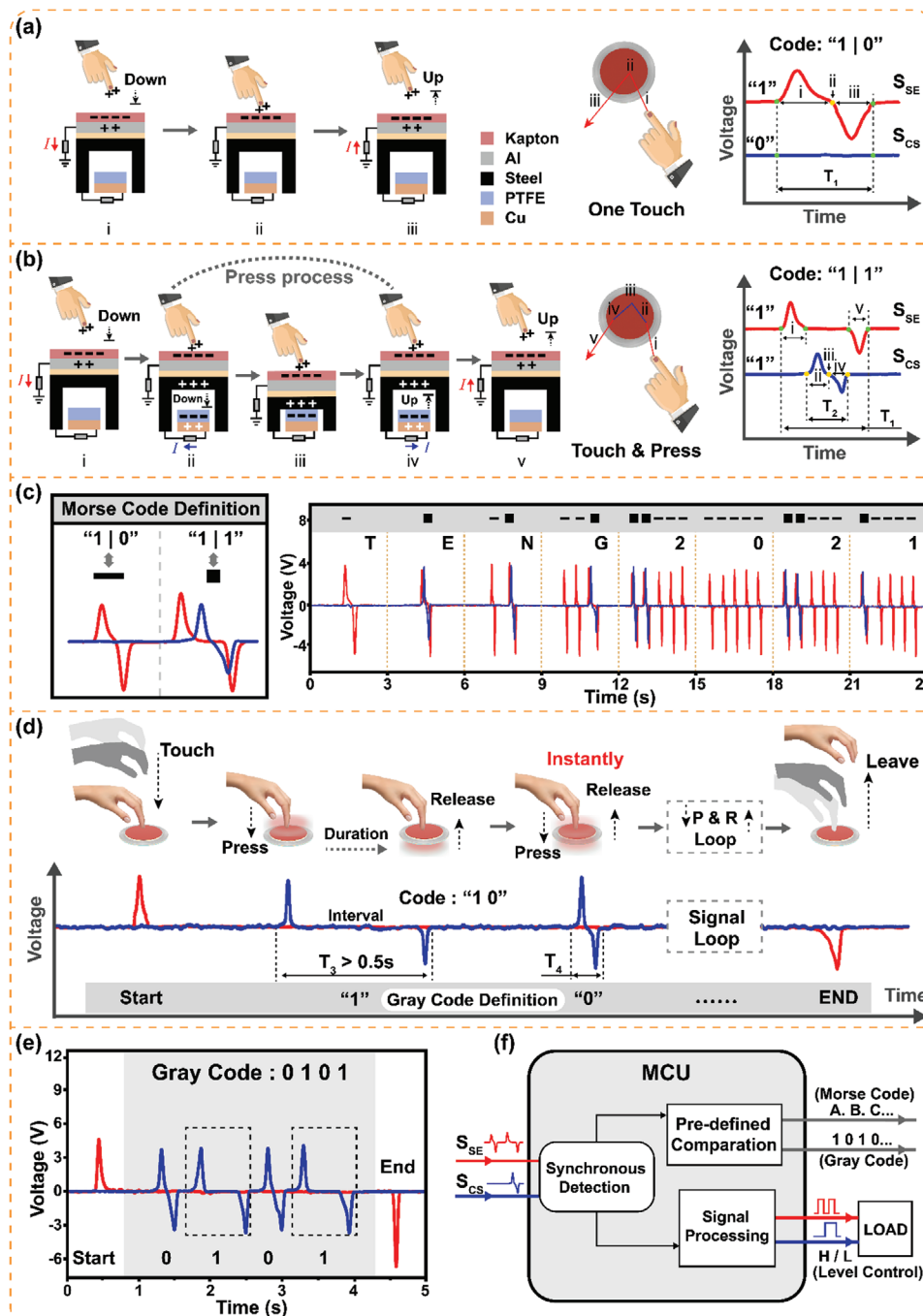


Figure 4. Information interaction and multiple signal mechanisms of SHC. a) Charge transfer path of SHC and signal of SE and CS electrical output coded as "1 | 0" when there is only a touch action. b) Charge transfer path of SHC and signal of SE and CS electrical output coded as "1 | 1" when there is the complete top-down touch and press action. c) Definition relationship between Morse code and two action codes: "1 | 0" defined as the dash of Morse code and "1 | 1" defined as the dot one, and the performance of the character "TENG2021" in the transmission process. d) Definition of Gray code and action electrical signal: touch signal is used as the start and end identification signal, the long press as "1", and the short press as "0". e) Transmission performance of Gray code "0101". f) SHC application preview: information interaction and load control.

synchronously follow the action sequence, which increases the information transmission capacity and security. Various combinations of touch and press actions can easily produce a variety of signals that represent more information. When the finger touches the SHC and then leaves, only SE signal is triggered

without the CS signal generated. Regarding the presence or absence of the signal as "1" and "0", then the code group of this action is "1 | 0" (Figure 4a). Similarly, when the finger completes the touch and press action then leaves (Figure 4b), both SE signal and CS signal are generated, so the code group is

"1 | 1". As the touch always starts before the press and ends last, the period T_1 of the touch signal is greater than the period T_2 of the press signal in both cases. The simplicity and effectiveness of conveying text information through these two actions have been discovered. Figure 4c describes the Morse code definitions of these two action code groups. The code group "1 | 0" is defined as the dash of Morse code, and the code group "1 | 1" is defined as the dot one. Based on this definition, an encoded string of "TENG2021" is decoded and captured successfully (Movie S1, Supporting Information).

Meanwhile, SHC also serves as a Gray code encoder to transmit a large amount of binary digital information. Figure 4d depicts the coding principle in this way. The SHC is pressed and held for a while and then released, the electrical signal generated by this action is defined as "1". In contrast, the electrical signal generated by the device being released instantly after being pressed is defined as "0". To reduce the bit error rate, the pressing duration T_3 of the former action is recommended to be longer than 0.5 s. A binary Gray code "0101" was successfully encoded and decoded by this coding rule (Figure 4e and Movie S2, Supporting Information). It should be noted that the finger needs keep in touch with the SHC during the whole encoding process of Gray code, till the end of it. The easily recognizable signal waveform confirms the reliability and efficiency of this definition.

Due to the stable performance of SE and CS signals and the successful verification of coding rules, the SHC has revealed its potential as a multifunctional encoder. The SHC is compared with other TENG-based coding devices in terms of structure, materials, coding methods, and signal characteristics (Figure S12, Supporting Information). It turns out that SHC does not use factors that are difficult to control as coding conditions, such as speed, frequency, contact area, and so on. This lowers the demands for encoding operations and reduces the bit error rate. The stable signal output makes the coding accuracy of SHC close to 100% without external interference. In the signal processing of the human-machine interface, SHC can alternately transmit codes of different rules without causing coherent interference. Specifically, the microcontroller unit (MCU) only needs to synchronously detect the two signals of the SHC, and then compare with the predefined code in the register to output Morse code text information or Gray code binary information. In addition to passing text signals, encoded signals from SHC are expected to be converted to high or low levels then to control electrical devices (Figure 4f).

2.5. Action Coding of SHC for Intelligent Control

To explore the potential application scenarios of SHC in-depth, it is necessary to design the correct action coding and signal processing circuits. First of all, a smart pilot lamp system (SPLS) was developed to perform danger warnings or prompt hazard removal using SHC action codes. It consists of four parts, as shown in Figure 5a, SHC as an action encoder, signal processor, brightness modulator, and pilot lamp. During the operation of the pilot lamp, it is controlled by the hybrid code groups, which are generated by touching and pressing the SHC. It has been designed two states for the system to work,

which are defined as danger and security respectively. In the danger state, the "1 | 0" hybrid code generated by touch will cause the brightness to sharply change to the next level. In the security state, touch action makes the light alternately gradually brighten or dim. Conveniently, the switching between these two states only needs to be pressed to generate the "1 | 1" code group. The realization of this function stems from the signal processor converting the original signals into H/L level signals, these level signals prompt the brightness modulator to perform pulse width modulation (PWM) to control the brightness changes of the pilot lamp (Figure 5b). Figures S13 and S14 (Supporting Information), respectively, provide the whole units' photo and circuit schematic diagrams of the entire system. Based on this, the self-made LED panel with the "TENG" pattern successfully works according to the defined mode. The code group "1 | 0" generated by the touch makes the brightness of the "TENG" lamp change sharply to prompt danger. Then the state was converted to a security reminder with the code group "1 | 1" generated by the press action. In this case, according to the "1 | 0" code group generated by the touch, the lamp gradually turns brighter and darker alternately to indicate that the danger is removed (Figure 5c and Movie S3, Supporting Information).

Next, the SHC is used to control the movement of the remote control car by taking advantage of its multiple action signal encoding. Figure 5d expresses the four main parts of this system, the coded SHC, signal processor, motor driver, and remote control car. When the system is working, the signal code group "1 | 0" generated by the touch action is used to start the car, and the remote control car will stop when the finger leaves. The touch-press action generated code group "1 | 1" will change the running direction of the vehicle after the next start. Figure 5e depicts the definition of motion coding and motion state and provides the level information of the processed original signals SSE and SCS. After the signal is converted into a radio frequency (RF) signal, a 1 kHz signal determines the forward rotation of the internal motor of the car. On the contrary, a 250 Hz signal will cause the motor to reverse. In this way, the car is selected to move forward or backward. Based on this SHC action code and control circuit design, a customized remote control car successfully moved according to a predetermined mode (Figure 5f and Movie S4, Supporting Information). Figures S15 and S16 (Supporting Information) provide the components of the remote control car control system and the schematic circuit diagram, respectively.

The successful realization of the above two applications not only proves the excellent multi-functional control ability of SHC, but also broadens the application horizons for the role of SHC in intelligent control. Moreover, it is expected to be further miniaturized and arrayed for development. More code combinations will bring more functions, which brings creative ideas to portable electronic devices.

3. Conclusion

In summary, the single-electrode and contact-separation working mode of TENG are integrated through an exquisite structural design, and a highly editable self-powered hybrid

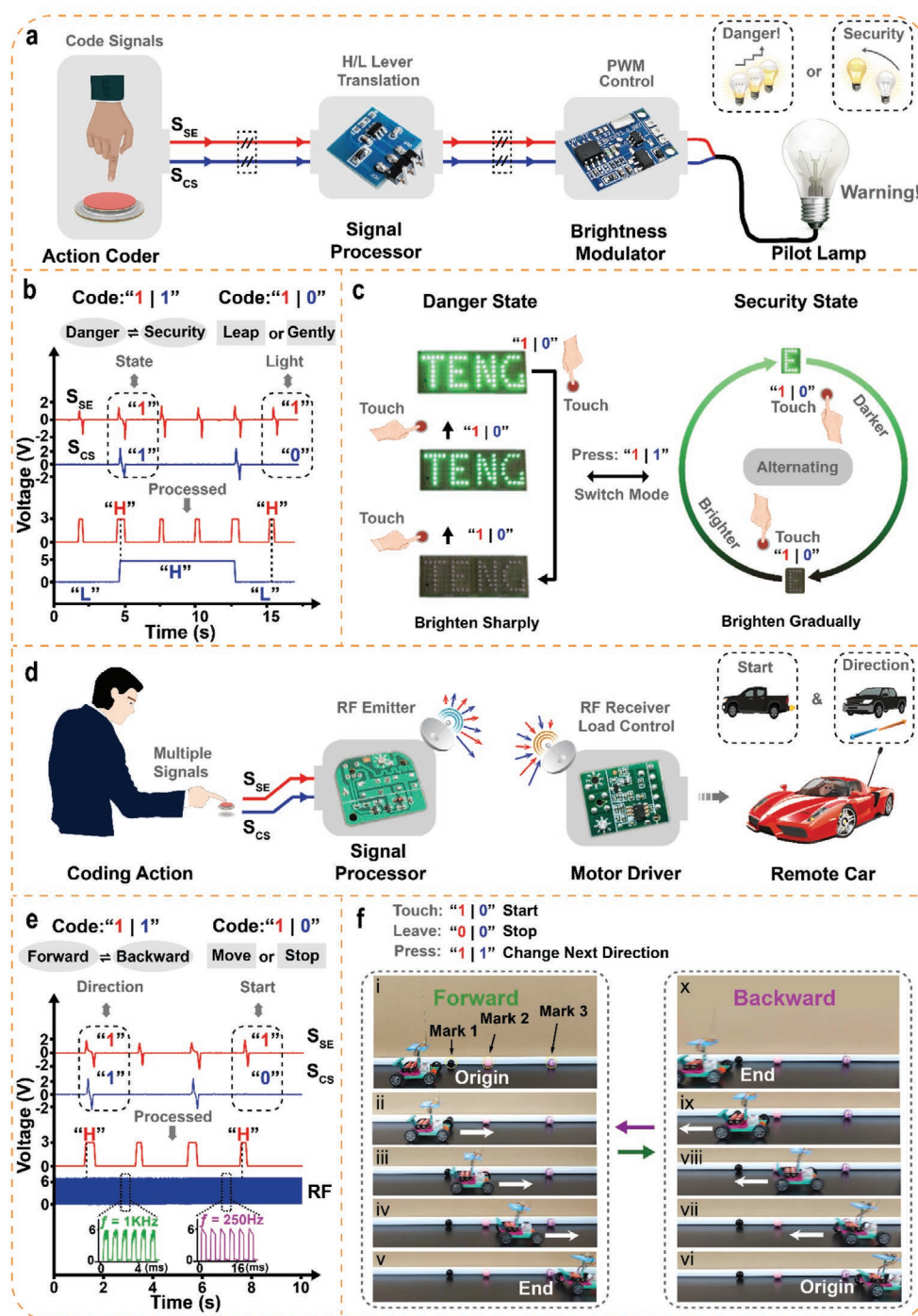


Figure 5. Applications of SHC. a) Flow chart of SHC involved in SPLS for the danger warnings or the security reminder. SPLS consists of four parts, SHC as an action encoder, signal processor, brightness modulator, and pilot lamp. b) Code definition in SPLS and signal processing. The code group "1 | 1" is used to switch the state of the lamp, danger warning or security reminder. The "1 | 0" code group is used to determine the brightness change of the lamp, brightness change with a leap manner in the danger warning state and brightness change with a gentle manner in the danger warning state. c) Demonstration of the smart pilot lamp in SHC control. In the danger warning state, brightness of the lamp changed sharply with the "1 | 0" code group. Then the danger warning was converted to a the security reminder with the code group "1 | 1", and brightness of the lamp changed gently with the "1 | 0" code group. d) Workflow of remote control vehicle based on SHC. e) Relationship between action signals and control command of remote control vehicle. The signal code group "1 | 0" generated by the touch action is used to start the car, and the signal code group "1 | 1" generated by touch-press action is used to change the running direction. f) The pictures captured of the remote control car under the control of SHC are in the process of moving in two directions.

triboelectric coder has been developed. Compared with the previously reported triboelectric interface, the developed SHC can detect multiple motion parameters and construct multiple hybrid coding signals. Stable structure makes the signal of SHC in independent and synergy working mode have absolute stability and reliability. In addition, through simple action definitions, the SHC can transmit information in the form of Morse code and Gray code as a hybrid coding platform, which reveal its sufficient advantage in information interaction. Moreover, the control of pilot lamp and remote control vehicle through the action code of SHC was successfully demonstrated. Besides, simple manufacturing methods and common materials are friendly to further miniaturization and array development. This highly editable and multi-parameter detection method has great potential in a variety of application scenarios such as 3D control, VR/AR, security systems, and portable electronic devices.

4. Experimental Section

Fabrication of SHC: The contact-separation part of the SHC was mainly composed of spring steel, PTFE, non-woven membrane, and PET. First, a piece of 50 μm thick PTFE film was washed with alcohol and deionized water, and then dried with nitrogen. Subsequently, the clean PTFE was sputtered by a Cu target in a vacuum for 20 min to form a dense copper film, under the conditions of DC power: 80 W and the flow rate of Ar gas was 40 sccm (DENTON, Discovery 635). In the second step, the treated PTFE and 0.2 mm thick PET used as the substrate were cut into circles with diameters of 10 and 20 mm, respectively, and the non-woven membrane (3M, 9448A, 0.16mm thick) was etched to the outer diameter 20 mm and 15mm inner diameter ring (VOIERN, WER1080). The third step is to assemble the spring steel, PTFE, non-woven ring, and PET support layer in the order from top to bottom, and the contact-separation part is completed. Among them, dome-shaped steel sheets (outer diameter 20 mm, inner diameter 14 mm, and thickness of 0.15 mm) were purchased from BONSDA (Shenzhen, China). Finally, the Kapton film (American Durafilm 100 μm) was combined with the adhesive aluminum foil to play the role of a single electrode part, and then they were closely attached to the upper surface of the steel by 3M tape to ensure the surface flatness.

Characterization and Measurement: The deformation and strain output test of the SHC was tested by the Motorized Test Stand (ESM303, Mark – 10) and the digital force gauge (HANDPI, CF – 500). The output performance of dual-mode TENG was measured and recorded by using an oscilloscope (HD 4096, Teledyne LeCroy) and an electrometer (6517B, Keithley). In the frequency and fatigue test, a PLA column was manufactured by the 3D printer (Raised3D, N2 plus) and driven periodically by a linear motor (E1100, LinMot,) to knock on the SHC. The SHC was fixed on the motor base or force gauge probe platform according to different experimental requirements. All SEM images were taken with a field emission scanning electron microscope (Nova NanoSEM 450, FEI). Optical micrographs were taken with an optical microscope (ECLIPSE LV100ND, Nikon) and digital sight (DS – U3, Nikon). The simulation of the motion state of the device is processed by COMSOL software, and the circuit diagram and circuit board are designed by OrCAD and PADS software, respectively.

Design of SHC Circuit in the Application of SPLS: In this design, the TTP118 chip was used to control the brightness of the light, seen in Figure S14 (Supporting Information). First, the signal in the contact-separation mode was processed by a charge amplifier and amplifying circuit, as well as a bistable circuit composed of a 4013 chip. The signal will recognize the press signal, and then switch the level between high and low, namely, “1” and “0”. They, respectively, determine whether the

brightness changes sharply or gradually. The single electrode signal was processed by TTP118 as a stable level signal. When there is a trigger, that is, when the level is “1”, PWM is directly performed to change the brightness. The level changes were synchronized with the action code groups “1 | 0” and “1 | 1”, so that the brightness of the light can be controlled.

Design of SHC Circuit in the Remote Control Car: To achieve radio control, the TX3E and the FMRX3MS wireless driver chips were used at the transmitter and receiver respectively, which determine that the farthest communication distance is about 20 m. as shown in Figure S16 (Supporting Information). First, the contact-separation signal outputs a stable voltage signal through an amplifier and a comparator, and then outputs a high or low level, that is, “1” and “0” through a bistable circuit. Press motion will switch the signal between the two. Then, “1” and “0” will control TX3E to emit 250 Hz and 1 kHz radio waves. FMRX3MS receives radio waves to drive the motor of the remote control car to rotate in the forward or reverse direction. The single electrode signal is pulled up to a stable level after trigger recognition processing. When the level is high, that is, “1”, the car starts. Therefore, the movement of the car can be controlled by the action codes “1 | 0” and “1 | 1”.

The experiments involving human subjects were performed with the full, informed consent of the volunteer, who is also a co-author of the manuscript. The exposed part of the device was made of non-toxic polymer materials and metal to ensure safety, and protective gloves were worn to volunteers. The all experiments were approved by Committee on Ethics of Beijing Institute of Nanoenergy and Nanosystems (A-2020012).

Supporting Information

Supporting Information is available from the Wiley Online Library or from the author.

Acknowledgements

This study was supported by the National Natural Science Foundation of China (61875015, T2125003, 32101117), the Strategic Priority Research Program of the Chinese Academy of Sciences (XDA16021101), the Beijing Natural Science Foundation (JQ20038, L212010), and the Fundamental Research Funds for the Central Universities.

Conflict of Interest

The authors declare no conflict of interest.

Author Contributions

Y.C. and Y.Y. contributed equally to this work. Z.L., B.S., and D.L. guided the project, conceived the idea, and designed the experiment. Y.C. and Y.Y. made the experiment, improved the scheme, and made writing plan. Y.C., Y.Y., and X.Q. collected data and edited videos. L.X. captured images and guided drawing. J.X. carried out software simulation. Y.C. and C.W. carried out force-electricity experiment. Y.C., Y.B., and Y.G. carried out the electrical characteristic work. Y.C. and Y.Y. drew the figures and prepared the manuscript. All authors discussed and reviewed the manuscript.

Data Availability Statement

The data that support the findings of this study are available from the corresponding author upon reasonable request.

Keywords

human-machine interaction, hybrid coder, self-powered sensors, TENG, triboelectric coder

Received: December 12, 2021
Published online:

- [1] S. Li, L. D. Xu, S. Zhao, *J. Ind. Inf. Integr.* **2018**, 10, 1.
- [2] S. Chen, H. Xu, D. Liu, B. Hu, H. Wang, *IEEE Internet Things J.* **2014**, 1, 349.
- [3] B. Dong, Q. Shi, Y. Yang, F. Wen, Z. Zhang, C. Lee, *Nano Energy* **2020**, 79, 105414.
- [4] Q. Shi, B. Dong, T. He, Z. Sun, C. Lee, *InfoMat* **2020**, 2, 1131.
- [5] D. Quesada-González, A. Merkoçi, *Biosens. Bioelectron.* **2017**, 92, 549.
- [6] B. Shih, D. Shah, J. Li, T. G. Thuruthel, Y.-L. Park, F. Iida, Z. Bao, R. Kramer-Bottiglio, M. T. Tolley, *Sci. Robot.* **2020**, 5, eaz9239.
- [7] J. Xiong, J. Chen, P. S. Lee, *Adv. Mater.* **2021**, 33, 2002640.
- [8] M. Ilami, H. Bagheri, R. Ahmed, E. O. Skowronek, H. Marvi, *Adv. Mater.* **2021**, 33, 2003139.
- [9] M. Venkatesan, H. Mohan, J. R. Ryan, C. M. Schürch, G. P. Nolan, D. H. Frakes, A. F. Coskun, *Cell Rep. Med.* **2021**, 2, 100348.
- [10] Y. Shi, F. Wang, J. Tian, S. Li, E. Fu, J. Nie, R. Lei, Y. Ding, X. Chen, Z. L. Wang, *Sci. Adv.* **2021**, 7, abe2943.
- [11] S. Mishra, Y.-S. Kim, J. Intarasirisawat, Y.-T. Kwon, Y. Lee, M. Mahmood, H.-R. Lim, R. Herbert, K. J. Yu, C. S. Ang, *Sci. Adv.* **2020**, 6, eaay1729.
- [12] M. J. Cima, *Nat. Biotechnol.* **2014**, 32, 642.
- [13] T. Q. Trung, N. E. Lee, *Adv. Mater.* **2016**, 28, 4338.
- [14] K. Sanderson, *Nature* **2021**, 591, 685.
- [15] P. Bach-y-Rita, S. W. Kercel, *Trends Cogn. Sci.* **2003**, 7, 541.
- [16] D. Valdes-Ramirez, M. A. Medina-Pérez, R. Monroy, O. Loyola-González, J. Rodríguez-Ruiz, A. Morales, F. Herrera, *IEEE Access* **2019**, 7, 48484.
- [17] J. Zhao, C. He, R. Yang, Z. Shi, M. Cheng, W. Yang, G. Xie, D. Wang, D. Shi, G. Zhang, *Appl. Phys. Lett.* **2012**, 101, 063112.
- [18] Q. He, Y. Wu, Z. Feng, C. Sun, W. Fan, Z. Zhou, K. Meng, E. Fan, J. Yang, *Nano Energy* **2019**, 59, 689.
- [19] Y. K. Pang, X. H. Li, M. X. Chen, C. B. Han, C. Zhang, Z. L. Wang, *ACS Appl. Mater. Interfaces* **2015**, 7, 19076.
- [20] M. Zhu, T. He, C. Lee, *Appl. Phys. Rev.* **2020**, 7, 031305.
- [21] F. R. Fan, W. Tang, Z. L. Wang, *Adv. Mater.* **2016**, 28, 4283.
- [22] Z. Liu, Y. Ma, H. Ouyang, B. J. Shi, N. Li, D. J. Jiang, F. Xie, D. Qu, Y. Zou, Y. Huang, H. Li, C. C. Zhao, P. C. Tan, M. Yu, Y. B. Fan, H. Zhang, Z. L. Wang, Z. Li, *Adv. Funct. Mater.* **2019**, 29, 1970017.
- [23] Y. Ma, Q. Zheng, Y. Liu, B. Shi, X. Xue, W. Ji, Z. Liu, Y. Jin, Y. Zou, Z. An, W. Zhang, X. Wang, W. Jiang, Z. Xu, Z. L. Wang, Z. Li, H. Zhang, *Nano Lett.* **2016**, 16, 6042.
- [24] H. Ouyang, J. Tian, G. Sun, Y. Zou, Z. Liu, H. Li, L. Zhao, B. Shi, Y. Fan, Y. Fan, Z. L. Wang, Z. Li, *Adv. Mater.* **2017**, 29, 1703456.
- [25] Y. Zou, P. Tan, B. Shi, H. Ouyang, D. Jiang, Z. Liu, H. Li, M. Yu, C. Wang, X. Qu, L. Zhao, Y. Fan, Z. L. Wang, Z. Li, *Nat. Commun.* **2019**, 10, 2695.
- [26] B. U. Hwang, J. H. Lee, T. Q. Trung, E. Roh, D. I. Kim, S. W. Kim, N. E. Lee, *ACS Nano* **2015**, 9, 8801.
- [27] J. Yang, J. Chen, Y. Su, Q. Jing, Z. Li, F. Yi, X. Wen, Z. Wang, Z. L. Wang, *Adv. Mater.* **2015**, 27, 1316.
- [28] Z. M. Wang, J. An, J. H. Nie, J. J. Luo, J. J. Shao, T. Jiang, B. D. Chen, W. Tang, Z. L. Wang, *Adv. Mater.* **2020**, 32, 2001466.
- [29] J. W. Liao, Y. Zou, D. J. Jiang, Z. Z. Liu, X. C. Qu, Z. Li, R. P. Liu, Y. B. Fan, B. J. Shi, Z. Li, L. Zheng, *Nano Energy* **2020**, 69, 104417.
- [30] H. Li, C. C. Zhao, X. X. Wang, J. P. Meng, Y. Zou, S. Noreen, L. M. Zhao, Z. Liu, H. Ouyang, P. C. Tan, M. Yu, Y. B. Fan, Z. L. Wang, Z. Li, *Adv. Sci.* **2019**, 6, 1801625.
- [31] M. Zhu, Z. Sun, Z. Zhang, Q. Shi, T. He, H. Liu, T. Chen, C. Lee, *Sci. Adv.* **2020**, 6, eaaz8693.
- [32] S. Wang, S. Liu, J. Zhou, F. Li, J. Li, X. Cao, Z. Li, J. Zhang, B. Li, Y. Wang, *Nano Energy* **2020**, 78, 105291.
- [33] C.-M. Chiu, S.-W. Chen, Y.-P. Pao, M.-Z. Huang, S.-W. Chan, Z.-H. Lin, *Sci. Technol. Adv. Mater.* **2019**, 20, 964.
- [34] Q. Shi, C. Qiu, T. He, F. Wu, M. Zhu, J. A. Dziuban, R. Walczak, M. R. Yuce, C. Lee, *Nano Energy* **2019**, 60, 545.
- [35] Q. Shi, Z. Zhang, T. Chen, C. Lee, *Nano Energy* **2019**, 62, 355.
- [36] H. Guo, H. Wang, Z. Xiang, H. Wu, J. Wan, C. Xu, H. Chen, M. Han, H. Zhang, *Adv. Funct. Mater.* **2021**, 31, 2103075.
- [37] Q. Shi, C. Lee, *Adv. Sci.* **2019**, 6, 1900617.
- [38] J. Chen, X. Wen, X. Liu, J. Cao, Z. Ding, Z. Du, *Nano Energy* **2021**, 80, 105446.
- [39] R. Cao, X. Pu, X. Du, W. Yang, J. Wang, H. Guo, S. Zhao, Z. Yuan, C. Zhang, C. Li, *ACS Nano* **2018**, 12, 5190.
- [40] D. H. Ho, J. Han, J. Huang, Y. Y. Choi, S. Cheon, J. Sun, Y. Lei, G. S. Park, Z. L. Wang, Q. Sun, *Nano Energy* **2020**, 77, 105262.
- [41] Q. J. Sun, X. H. Zhao, C. C. Yeung, Q. Tian, K. W. Kong, W. Wu, S. Venkatesh, W. J. Li, V. A. L. Roy, *ACS Appl. Mater. Interfaces* **2020**, 12, 37239.
- [42] F. Yu, J. C. Cai, L. Zhu, M. Sheikhi, Y. H. Zeng, W. Guo, Z. Y. Ren, H. Xiao, J. C. Ye, C. H. Lin, A. B. Wong, T. Wu, *ACS Appl. Mater. Interfaces* **2020**, 12, 26258.
- [43] H. Zhou, D. X. Li, X. M. He, X. D. Hui, H. Y. Guo, C. G. Hu, X. J. Mu, Z. L. Wang, *Adv. Sci.* **2021**, 8, 2101020.
- [44] A. Chandrasekhar, V. Vivekananthan, G. Khandelwal, S. J. Kim, *Nano Energy* **2019**, 60, 850.
- [45] J. Chen, X. J. Pu, H. Y. Guo, Q. Tang, L. Feng, X. Wang, C. G. Hu, *Nano Energy* **2018**, 43, 253.
- [46] H. Zou, Y. Zhang, L. Guo, P. Wang, X. He, G. Dai, H. Zheng, C. Chen, A. C. Wang, C. Xu, *Nat. Commun.* **2019**, 10, 1427.
- [47] S. Wang, L. Lin, Z. L. Wang, *Nano Lett.* **2012**, 12, 6339.
- [48] G. Zhu, W. Q. Yang, T. Zhang, Q. Jing, J. Chen, Y. S. Zhou, P. Bai, Z. L. Wang, *Nano Lett.* **2014**, 14, 3208.